Inorganic Chemistry

Article

pubs.acs.org/IC

Metal-Assisted Ligand-Centered Electrocatalytic Hydrogen Evolution upon Reduction of a Bis(thiosemicarbazonato)Cu(II) Complex

Andrew Z. Haddad, Steve P. Cronin, Mark S. Mashuta, Robert M. Buchanan, and Craig A. Grapperhaus*

Department of Chemistry, University of Louisville, 2320 South Brook Street, Louisville, Kentucky 40292, United States

Supporting Information

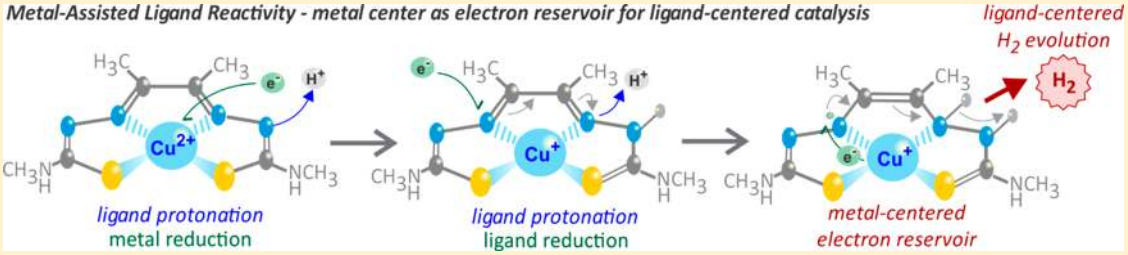

ABSTRACT: In this study, we report the electrocatalytic behavior of the neutral, monomeric Cu(II) complex of diacetyl-bis(*N*-4-methyl-3-thiosemicarbazonato), CuL^1, for metal-assisted ligand-centered hydrogen evolution in acetonitrile and dimethylformamide. CuL^1 displays a maximum turnover frequency (TOF) of 10 000 s^{-1} in acetonitrile and 5100 s^{-1} in dimethylformamide at an overpotential of 0.80 and 0.76 V, respectively. The rate law is first-order in catalyst and second-order in proton concentration. Gas analysis from controlled potential electrolysis confirms CuL^1 as an electrocatalyst to produce H_2 with a minimum Faradaic efficiency of 81% and turnover numbers as high as 73 while showing no sign of degradation over 23 h. The H_2 evolution reaction (HER) was probed using deuterated acid, demonstrating a kinetic isotope effect of 7.54. A proton inventory study suggests one proton is involved in the rate-determining step. Catalytic intermediates were identified using ^{1}H NMR, X-ray photoelectron, and UV−visible spectroscopies. All catalytic intermediates in the proposed mechanism were successfully optimized using density functional theory calculations with the B3LYP functional and the 6-311g(d,p) basis set and support the proposed mechanism.

INTRODUCTION

Rising energy demands coupled with growing concerns of repercussion from global climate change have ignited considerable interest in the development of carbon neutral energy systems.[1−3] Hydrogen is a promising component of these systems, representing a lightweight, energy dense energy carrier. Hydrogen evolution reactions (HERs), which involve a two-electron reduction of protons, can be used to store energy in H_2, with subsequent energy release through hydrogen oxidation reactions (HORs).[4−6] Platinum is an excellent catalyst for HERs and HORs,[7] yet its scarcity and high costs limit practical large scale application, leading to the pursuit of sustainable and inexpensive homogeneous and heterogeneous materials many which employ earth abundant first-row transition metals.[8−21] One of these promising systems are the pendant-base bis(diamine) nickel complexes of Dubois and Bullock, which proceed with the participation of a crucial metal-hydride intermediate.[22−26] Following this cue from nature, many others have employed the metal-hydride approach to generate HER catalysts that operate via similar hydride-based mechanisms.

Traditional HER catalysis follows a metal-centered route, employing a transition metal capable of accommodating multiple oxidation states for the two-electron hydride transfer associated with hydrogen evolution. There is an emerging interest in the use of redox-active ligands that open alternate HER routes, including ligand-assisted metal-centered,[27] ligand-centered,[28−30] and metal-assisted ligand-centered reactivity,[31,32,29] Scheme 1.

Among the latter two of these three classes, the ligand can often participate in redox events either in an implicit or explicit nature.[33] Due to their ability to act as electron reservoirs, redox noninnocent ligands can drastically alter reactivity and enhance catalytic properties of transition-metal complexes, which have made them attractive candidates in the field of catalysis.[33−35] Small molecule transition-metal complexes featuring redox noninnocent ligands thus have garnered considerable interest among many fields of catalysis, including water oxidation,[36,37] alcohol oxidation,[38] carbon dioxide activation,[39] hydrogen evolution,[15,27−29,31,32,40] and hydrogen oxidation.[41]

The redox noninnocent formalism can be traced back to the early work by Jørgensen, when in 1966 he termed ligands as either innocent or noninnocent in an attempt to avoid confusion when describing whether a ligand allowed the oxidation state of the central atom to be identified.[42] Further

Received: June 27, 2017
Published: August 31, 2017

DOI: 10.1021/acs.inorgchem.7b01608
Inorg. Chem. 2017, 56, 11254−11265

Scheme 1. Overview of Reactivity Using Noninnocent Ligands

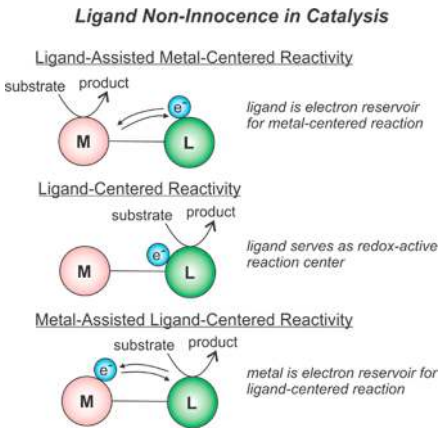

inquiries into exploiting catalysis using noninnocent ligands intensified upon the discovery of metal-radical locales in the active sites of several metalloenzymes such as galactose oxidase and hydrogenase, both which implicate ligand noninnocence as a crucial factor in their activity.[43−45] The thiosemicarbazone ligand classification as a redox active ligand has been well-documented,[38,46−49] and can stabilize low oxidation states of many metal complexes such as nickel iron and copper due to their soft N_2S_2 or N_3S donor sets, making them attractive candidates for studying catalytic reactions with these metals.

The first nontransition-metal homogeneous HER catalyst reported was an aluminum-bis(imino)pyridine complex by Thompson et al. that evolves H_2 with a TOF of 3.3 h^{-1} and with an overpotential of 0.5 V via ligand-centered reduction and protonation events.[29] Haddad et al. reported a rhenium dithiolate complex as the first reversible, ligand-centered catalyst for both HER and HOR, which proceeds through a radical coupling mechanism,[32,50] while Solis et al. reported a nickel phlorin intermediate with a hydridic C−H bond that reacts with an external acid to produce H_2 in a purely ligand-centered process.[51] Following these reports, Zarkadoulas et al. reported DFT computations that suggested Ni-dithiolene HER catalysts may proceed via metal-hydrides or a ligand-centered mechanism.[15]

Recently, we reported the first example of catalytic HER with the noninnocent bis(thiosemicarbazone) ligand framework, Scheme 2.[28] The zinc complex of diacetyl-bis(*N*-4-methyl-3-thiosemicarbazone), ZnL^1, catalyzes HER with a maximum TOF of 1170 s^{-1}. The HER mechanism was established through a rigorous protocol involving kinetic studies, including digital simulations of electrochemical data, DFT computations of catalytic intermediates, and location of the transition state. Results indicate a ligand-centered process involving a binuclear transition state with evolution of H_2 via ligand hydride-proton coupling. Notably, the free ligand H_2L^1 also demonstrates similar HER activity. Very recently, Straistari et al. reported HER activity with a related bis(thiosemicarbazonato)Ni(II) complex with an enhanced TOF of 3080 s^{-1}, proposed to involve initial ligand-centered reduction and protonation followed by metal-centered reduction.[52]

Scheme 2. Thiosemicarbazone-Based HER Electrocatalysts

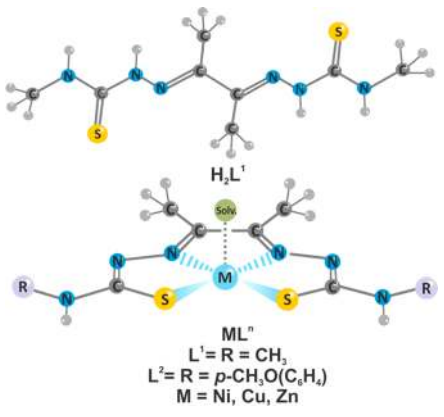

In this study, we continue our pursuit of alternate HER strategies with the report of metal-assisted ligand-centered HER catalysis using the copper complex of diacetyl-bis(*N*-4-methyl-3-thiosemicarbazone), CuL^1, Scheme 2. The electrochemistry of CuL^1 was previously investigated by both Mauer et al. in 2002[53] and Holland et al. in 2008[54] during its study as a radiopharmaceutical agent for the diagnosis of hypoxia. Notably, Holland and co-workers observed a reduction at −1.007 V vs SCE in the presence of HBF_4 that they assigned to the reduction of protons. This was supported by the presence of small bubbles, which was attributed to hydrogen formation, at the Pt working electrode upon prolonged reduction. Herein, we report a detailed investigation of CuL^1 in the presence of acetic acid that conclusively demonstrates electrocatalytic HER activity. Evaluation of the mechanism by electrochemical, spectroscopic, and density functional theory (DFT) methods supports a metal-assisted ligand-centered pathway.

EXPERIMENTAL SECTION

Electrochemical Methods. All cyclic voltammetry (CV) and controlled potential coulometry (CPC) measurements were recorded using a Gamry Interface potentiostat/galvanostat which was connected to a glassy carbon working electrode (6.5 mm diameter, surface area = 0.07 cm^2), a platinum wire counter electrode, and Ag/AgCl reference electrode. Before use, the working electrode was polished using an aqueous alumina slurry. The working and counter electrodes were cleaned before use by washing with water, ethanol, isopropanol, and acetone and then sonication for 10 min in acetonitrile/DMF. CV measurements were conducted using a three-neck electrochemical cell that was washed and dried in an oven overnight before use. All electrochemical experiments were conducted under a N_2 atmosphere. All CPC measurements were conducted using a two-chambered glass electrolysis cell with working and auxiliary compartments separated by a frit with a volume of 10 mL in each, washed and dried the night before use. The working compartment was fitted with a glassy carbon working electrode and an Ag/AgCl reference electrode. The auxiliary compartment was fitted with a Pt wire counter electrode. The working compartment contained 0.292 M acetic acid added to a 0.1 M Bu_4NPF_6 acetonitrile or DMF solution, while the auxiliary compartment was filled with 0.1 M Bu_4NPF_6 acetonitrile or DMF solution. Both compartments were purged for 15 min with N_2 prior to electrolysis. A control (blank) CPC study was conducted and subtracted from experimental results (Supporting Information). Electrolysis measurements were performed after addition of 0.6 mM CuL^1 to the working compartment for several time durations. The evolved gas was subjected to gas chromatography thermal conductivity (GC-TCD) analysis at the end of the electrolysis using a Gow-Mac series 400 GC-TCD equipped with a molecular sieve column for product detection. The column was heated to 130 °C under N_2 gas flow with 250 μL injection samples injected onto the column to confirm H_2 as the gaseous product.

Overpotential Determination. Overpotential can be defined as the difference between the thermodynamic and equilibrium potentials

DOI: 10.1021/acs.inorgchem.7b01608
Inorg. Chem. 2017, 56, 11254−11265

for a given reaction and the potential at which the reaction occurs under a set of specific conditions. The accurate determination of overpotential requires an estimation of $E_{cat/2}$ and E_{ref} ($E^T_{1/2}$), each of which can change, depending on the reaction conditions. The value for the potential for catalysis should be related to the catalytic current, and therefore, we use $E_{cat/2}$. E_{ref} is the half-wave potential of the most acidic couple in solution. This value is based on the standard potential of proton reduction in the solvent E°_{H}/H_2. Using the methods of Artero,[55] E_{ref} is calculated using eq 1, which allows for calculation of the overpotential (η) for proton reduction by CuL^1 under some specific experimental conditions.

$$E^T_{1/2} = E^\circ_{H^+/H_2} - \frac{2.303xRT}{F}pK_a + \varepsilon_D - \frac{RT}{2F}\ln\frac{C_0}{C^\circ_{H_2}} \quad (1)$$

The overpotential can then be estimated as $\eta = |(E_{ref} - E_{cat/2})|$ (see Supporting Information for all sample calculations).

Faradaic Efficiency Determination. Evolved gas from the cathode compartment displaced water in a cylinder with radius 1.12 cm by a height of 2.16 cm. Using the equation for the volume of a cylinder, $V = \pi(r)^2h$, we can calculate the volume displaced. This is calculated to be 8.51 mL. Using the conversion factor of 24.0 L of any ideal gas per one mole of gas at room temperature allows us to quantify the number of moles of H_2 evolved as 3.56×10^{-4} moles. This value can then be compared to the theoretical number of moles of H_2 evolved based on total charge passed, determined to be 4.40×10^{-4}. Faradaic efficiency is defined as moles of H_2 quantified/mol of H_2 theoretical based on charge × 100%. This corresponds with a minimum Faradaic efficiency of 81.0% (Supporting Information).

Turnover Frequency Determination.

$$i_{cat} = nFA[cat]\sqrt{Dk[H^+]^2} \quad (2)$$

Eq 2 details the relationship between the catalytic current i_{cat}, the catalyst concentration [cat], and the acid concentration $[H^+]$ for a catalytic reaction that is second-order in acid and first-order in catalyst.[56] The terms n, F, A, and D are the normal electrochemical terms related to the number of electrons transferred, Faraday's constant, area of the electrode (0.07 cm^2), and diffusion constant, respectively.

Eq 2 (Randle–Sevcik equation) provides the relationship between the peak current (i_p), catalyst concentration, and scan rate (ν) in the absence of acid. The factor of 0.4463 is related to the diffusion equations;[57] R is the gas constant, and T is temperature in K. The other terms are the same as in eq 1. Application of eq 3 was used for the construction of Cottrell plots (Figure 1) and determination of the CuL^1 diffusion coefficient.

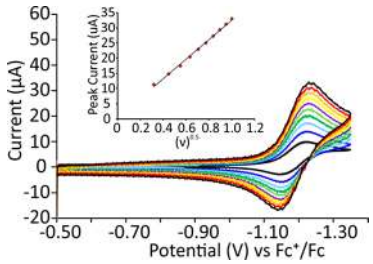

Figure 1. CVs of CuL^1 in 0.1 M Bu_4NPF_6 ACN solution at scan rates of 0.1 (black), 0.2 (blue), 0.3 (light blue), 0.4 (green), 0.5 (light green), 0.6 (purple), 0.7 (yellow), 0.8 (orange), 0.9 (red), and 1.0 (black) V/s.CuL^1. Inset: Cottrell plot of peak current vs square root of scan rate.

$$i_p = 0.4463FA[cat]\sqrt{\frac{F\nu D}{RT}} \quad (3)$$

Thus, the ratio of i_{cat}/i_p (eq 4) is obtained from the quotient eqs 1 and 2.

$$\frac{i_{cat}}{i_p} = \frac{n}{0.4463}\sqrt{\frac{RTk[H^+]^2}{F\nu}} \quad (4)$$

Under pseudo first-order conditions where $k_{obs} = k[H^+]^2$, eq 4 simplifies to 5.[58]

$$\frac{i_{cat}}{i_p} = \frac{n}{0.4463}\sqrt{\frac{RTk_{obs}}{F\nu}} \quad (5)$$

Eq 5 can be simplified further to eq 6, when $n = 2$, and when at scan rate independent conditions can be used to estimate the observed rate constant or turnover frequency (TOF) (see Supporting Information for sample calculations).

$$k_{obs} = 1.94\nu\left[\frac{i_{cat}}{i_p}\right]^2 \quad (6)$$

Eqs 2–6 are used for TOF estimation for electrocatalysts under "pure kinetic conditions" where plateau current is easily observable as an S-shaped wave that is scan rate independent.[59] The CVs reported in this manuscript show plateau current at low acid concentrations that are scan rate independent. Upon increasing substrate concentration, data collected under scan rate independent conditions no longer display S-shaped waves, making current plateaus increasingly more difficult to observe. This is attributed to the proximity of the catalytic wave to the edge of the solvent window. Foot of the wave analysis (FOWA) is an alternate method to determine TOF that was developed specifically for electrocatalysts that do not operate under pure kinetic conditions.[60,61] FOWA was developed for electrocatalysts in which the first step involves electron transfer (i.e., EECC or ECEC) and its application requires an accurate measurement of $E_{1/2}$ for the catalyst in the absence of substrate. However, the HER mechanism for CuL^1 involves an initial protonation step (CECE) such that it is not possible to measure $E_{1/2}$ of the catalyst in the absence of substrate. Given this complication, TOF values were determined using plateau current analysis (eqs 2–6) despite the absence of S-shaped waves. As noted by Dempsey in a recent review,[59] plateau current analysis "cannot be rigorously applied" under these conditions, but it "can be useful in an initial assessment of catalyst performance because even current enhancements for non-ideal waves are reflective of catalysis." Further, she notes that in such cases, the plateau current method "generally underestimates the rate constant."[59]

X-ray Photoelectron Spectroscopy of Electrode Adsorbed Films. CPEs of 0.6 mM CuL^1 with 0.292 M acetic acid added in 0.1 M Bu_4NPF_6 DMF and ACN solutions were run for 23.5 and 4.2 h, respectively. After completion of electrolysis, the working electrode was removed and washed with DI water. A visible red-brown film persisted on the electrode surface. The films were scraped off using a spatula, collected onto wax paper, and transferred to a glass vial, which was sealed and wrapped with parafilm. XPS analysis was conducted by the Nanoscale Characterization Facility at the University of Indiana (Bloomington, IN) using a PHI VersaProbe II Scanning X-ray Microprobe system.

Computational Methods. Initial benchmark calculations were performed using M06, B3LYP, and B97-D.[62−67] On the basis of the energetic minima results, B3LYP was chosen for use as the functional for subsequent calculations. Optimizations were performed in the gas phase using DFT employing the B3LYP exchange correlation functional and the 6-311G(d,p) basis set for all atoms as implemented in the Gaussian09 suite of programs for electronic structure,[68] and ChemCraft was used for graphics visualization.[69] All optimizations were performed under tight constraints with no symmetry imposed. All input coordinates are available in the Supporting Information.

NMR Spectroscopy of $[CuL^1H_2]^+$. A 5 mL solution of 8.9 mM CuL^1 in DMSO-d_6 was prepared in an Ar filled glovebox. To this solution was added 10 mg of bis(cyclopentadienyl)cobalt(II). The solution was stirred for 15 min during which time the solution changed

DOI: 10.1021/acs.inorgchem.7b01608
Inorg. Chem. 2017, 56, 11254−11265

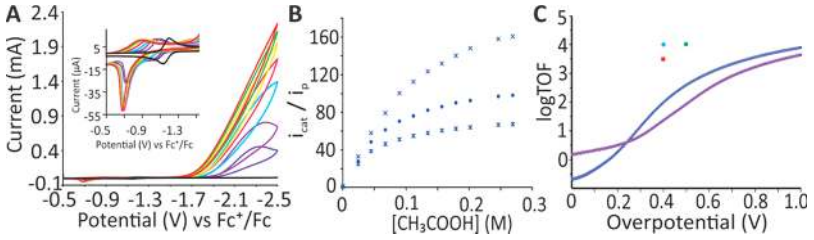

Figure 2. (A) CVs of 0.6 mM CuL^1 (black) in 0.1 M Bu_4NPF_6 ACN with 0.0244 (purple), 0.0448 (light purple), 0.0896 (light blue), 0.134 (pink), 0.179 (yellow), 0.244 (light green), and 0.269 (red) M CH_3COOH, Inset: Blow up of CV showing shift of $Cu^{II/I}$ reduction event. (B) Plot of i_{cat}/i_p vs $[CH_3COOH]$ for 0.60 mM CuL^1 (blue) at scan rates of 0.20 (X), 0.50 (●) and 1.00 (*) V/s. (C) Catalytic Tafel plot of CuL^1 in ACN (blue) and in DMF (purple) with comparison of performance for hydrogen evolution with those of others reported in literature. Blue ♦: $Co^{II}(dmgH)_2py$; green ●: $[Ni(P_2^{Ph}N^{Ph})_2]^{2+}$; red ■: NiL^2; magenta.[61]

color from red to light purple. A 700 μL portion of the resulting solution was transferred to an NMR tube and capped for analysis. A second 700 μL portion was transferred to an NMR tube followed by addition of 2 μL of aqueous HPF_6 (55 wt %). Data were collected on a Varian 400 MHz NMR. Reduction of CuL^1 to $[CuL^1]^-$ by cobaltocene was confirmed by UV−vis measurements. In a round-bottom flask 19 mg of CuL^1 was dissolved in 30 mL of deoxygenated DMF under N_2. An aliquot was removed, and the spectrum was recorded. Then, 1 equiv of bis(cyclopentadienyl)cobalt(II) was added, and the solution was stirred for 15 min. Finally, 2 equiv of aqueous HPF_6 (55 wt %) was added. An aliquot was removed, and the spectrum was recorded.

RESULTS AND DISCUSSION

Synthesis and Electrochemical Characterization. The CuL^1 compound was isolated as an air-stable burgundy solid from H_2L^1 and copper(II) acetate as previously reported by Dilworth et al.[70,71] The cyclic voltammogram (CV) of CuL^1 in acetonitrile (ACN) or dimethylformamide (DMF) containing 0.1 M Bu_4NPF_6 as supporting electrolyte displays a reversible $Cu^{II/I}$ event at −1.20 V vs ferrocenium/ferrocene (Fc^+/Fc), consistent with prior reports. Additional CV data collected at multiple scan rates from 0.1 to 1.0 V/s in ACN (Figure 1) and DMF (data not shown) were used to construct Cottrell plots (Figure 1, inset), establishing that the $Cu^{II/I}$ reduction is diffusion limited, thus demonstrating the potential of CuL^1 as a homogeneous electrocatalyst. The slope of the plot yields a diffusion coefficient of 7.9×10^{-6} cm^2/s in ACN and 9.35×10^{-6} cm^2/s in DMF. The formal $Cu^{III/II}$ couple was observed at 0.24 V vs Fc^+/Fc in DMF and ACN in line with prior reports, but this event was not further evaluated in the current study.

Homogeneous Catalytic Hydrogen Evolution: Cyclic Voltammetry and KIE. Addition of acetic acid exceeding 0.024 M to 0.6 mM ACN solutions of CuL^1 shifts the $Cu^{II/I}$ reduction potential from −1.20 to −0.95 V and introduces a catalytic cathodic current at −1.70 V vs Fc^+/Fc (Figure 2A). The +0.25 V shift is consistent with protonation prior to the initial electrochemical reduction and is consistent with previously reported results with CuL using the strong acid HBF_4.[32,54] Single protonation prior to reduction was confirmed through UV−visible spectroscopy analysis, vide infra. The ratio of the catalytic current to the peak current displays linear dependence on the acid concentration up to 0.157 M, indicating a second-order dependence of the catalytic rate on the acid concentration.[72] At concentrations greater than 0.157 M, the current response begins to plateau, reaching an acid independent region at concentrations of 0.269 M, (Figure 2B). This transition from second-order to zero-order dependence requires a pre-equilibrium step(s) involving two protons that precedes the rate-determining step for H_2 elimination. The current becomes scan rate independent at 0.2 V/s. CVs run at higher scan rates result in a decrease of current response; therefore, values reported for CuL^1 are based on current response at 0.2 V/s. Under these conditions the i_p of the $Cu^{II/I}$ reduction event, 14.0 μA, and the i_{cat} max from the acid-independent region, 2.25 mA at an overpotential of 0.8 V, correspond with a maximum i_{cat}/i_p value of 161, affording a TOF of 10 000 s^{-1}.[55,60,73,74] While the maximum TOF is substantial, its merit is severely diminished by the large overpotential of 0.8 V required (Figure 2C).

The electrocatalytic activity of 0.6 mM CuL^1 with acetic acid was also assessed in DMF. Previous electrochemical studies in DMF indicated that acetic acid does not protonate CuL^1 at concentrations up to 0.022 M acetic acid.[53] However, an increase in current at −1.9 V vs Fc^+/Fc is observed upon increasing additions of acetic acid at higher concentrations (Figure 3A). At concentrations of acid greater than 0.292 M, the current saturates reaching a maximum i_{cat} of 1.49 mA (Figure 3A inset). Acid addition results in a shift of the $Cu^{II/I}$ potential from −1.20 to −0.95 V, as observed in ACN, attributed to a single protonation event prior to reduction. Catalytic current becomes independent of scan rate above 1.0 V/s (Figure 3B). Under these conditions i_{cat} is 1490 μA

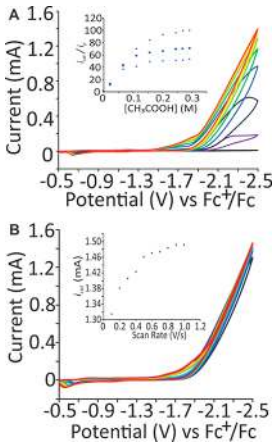

Figure 3. (A) CVs of 0.6 mM CuL^1 (black) in 0.1 M Bu_4NPF_6 DMF with 0.0244 (purple), 0.0672 (dark purple), 0.112 (blue), 0.157 (green), 0.202 (light green), 0.246 (yellow), 0.269 (orange), and 0.292 (red) M CH_3COOH. (inset) Plot of i_{cat}/i_p vs $[CH_3COOH]$ for 0.6 mM CuL^1 at scan rates of 0.20 (♦), 0.50 (■), and 1.00 (▲) V/s. (B) CVs of 0.6 mM CuL^1 (black) in 0.1 M Bu_4NPF_6 DMF with 0.292 M CH_3COOH at scan rates from 0.1 to 1.0 V/s. (inset) Plot of i_{cat} vs scan rate for 0.6 mM CuL^1 in 0.1 M Bu_4NPF_6 DMF with 0.292 M CH_3COOH.

DOI: 10.1021/acs.inorgchem.7b01608
Inorg. Chem. 2017, 56, 11254−11265

(overpotential = 0.76 V), and i_p is 29 μA, giving a TOF of 5100 s^{-1}, which is significantly lower than the TOF in ACN.

The Tafel plot of the log TOF versus overpotential for CuL^1 (Figure 2C) displays the TOF as a function of the applied overpotential.[61] At high overpotentials CuL^1 displays high logTOF values, reaching a maximum of 3.99. CuL^1 maintains a logTOF value greater than one, only with applied overpotentials greater than 0.25 V. As previously noted, the maximum logTOF for CuL^1 of 3.99 requires a large overpotential of 0.8 V. Comparatively, state-of-the-art metal-hydride HER electrocatalysts, such as nickel-bis(diphosphine) and cobaloxime exhibit logTOF values of 4.00 at overpotentials of 0.50 and 0.40 V, respectively.[61] Our previously reported ligand-centered electrocatalysts ZnL^1 and H_2L^1 have lower maximum logTOF values than CuL^1, and achieve logTOF values of 3.06 and 3.12 at overpotentials of 0.75 and 1.4 V, respectively.[28] Artero's related NiL^2 electrocatalyst achieves a maximum logTOF of 3.50 at an overpotential of 0.4 V, similar to the state-of-the-art metal-hydride HER catalysts.[52]

Analysis of the CVs of CuL^1 under catalytic HER conditions reveal a new oxidation event at a potential of −0.65 V Fc^+/Fc during the return anodic scan (Figure 2A inset), which is assigned to the Cu(II/I) couple of the diprotonated copper(I) intermediate, $[CuL^1H_2]^+$. This event is 300 mV more positive than the Cu(II/I) couple of the monoprotonated $[CuL^1H]^+$, which in turn is 250 mV more positive than the CuL^1. The intensity of the peak current at −0.65 V demonstrates scan rate dependence typical of diffusion controlled behavior (Figure 3B), confirming it is not due to an adsorbed species.

As noted above, the catalysis is second-order in acid in the acid dependent regime. To determine the order with respect to the catalyst, the concentration of CuL^1 was varied from 0.1 to 1.0 mM in solution containing 0.15 M acetic acid. A plot of catalyst concentration versus peak current reveals a linear relationship, confirming a first-order dependence on the concentration of the catalyst (Supporting Information) and an overall third-order process.

To further evaluate the HER mechanism of CuL^1, the H/D kinetic isotope effect (KIE) was measured. CuL^1 displays a large KIE of 7.54 using 100% CD_3CO_2D. The high KIE value observed when using 100% CD_3CO_2D is distinct from the inverse KIEs reported for some HER catalysts proceeding through metal-hydrides[75] but similar to that observed for a ligand-centered Rethiolate HER catalyst.[32] Because CuL^1 HER catalysis is second-order in $[H^+]$, a proton inventory study was conducted to determine the number of protons involved in the rate-determining step.[76] Cyclic voltammograms collected with variable quantities of CH_3CO_2H and CD_3CO_2D were used to generate plots of KIE versus the percent fraction of CD_3CO_2D (Figures 4A and B). The plot yields a linear fit consistent with the involvement of a single proton in the rate-determining step.

Controlled Potential Electrolysis. A series of controlled potential electrolysis (CPE) experiments was performed using 0.6 mM CuL^1 and 0.292 M acetic acid with potential held at −1.65 V vs Fc^+/Fc, in both DMF and ACN (Table 1). Electrolysis in 0.1 M Bu_4NPF_6 DMF solutions was allowed to run for 84 400 s (23.4 h), resulting in a total charge passed of 85.0 C, corresponding to 4.4×10^{-4} moles of H_2 produced with a turnover number (TON) of 73.3. Gas analysis of the headspace using GC-TCD confirms H_2 as the gaseous product (Supporting Information). The charge increases linearly over time with no signs of degradation or decrease in activity over 23 h (Figure 5). A second CPE in DMF over 72 120 s (20 h)

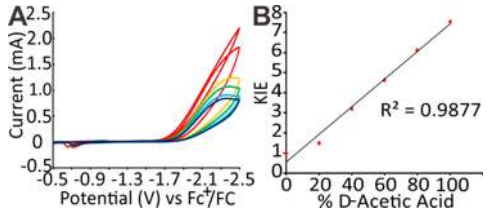

Figure 4. (A) CVs of 0.6 mM CuL^1 in 0.1 M Bu_4NPF_6 ACN solution with 0.269 M acetic acid at 0 (dark red), 20 (red), 40 (yellow), 60 (green), 80 (light blue), and 100 (dark blue) mole % of CD_3COOD. (B) Plot of KIE vs % CD_3COOD.

Table 1. Summary of CPE Results

entry[a]	solvent[c,d]	duration (S^{-1})	charge (C)	moles of H_2 produced ($\times 10^{-4}$)	TON
1	ACN	15 000	60.4	3.1	52
2	ACN	13 000	84.7	4.4	73
3	DMF	84 400	67.0	3.5	58
4	DMF	72 120	85.0	4.4	73[b]

[a]Overpotential 0.8 V vs Fc^+/Fc for all CPEs. [b]Faradaic efficiency 81% (see Supporting Information). [c]Blank run of 0.292 M acetic acid in DMF yields 68.2 mC. [d]Blank run of 0.292 M acetic acid in ACN yields 57.6 mC.

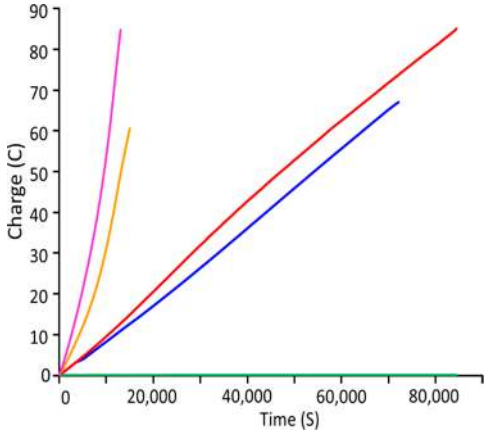

Figure 5. CPE of 0.6 mM CuL^1 in 0.1 M Bu_4NPF_6 ACN (pink and orange) or 0.1 M Bu_4NPF_6 DMF (red and blue) solutions with 0.292 M CH_3COOH added; 0.1 M Bu_4NPF_6 DMF with 0.292 M CH_3COOH, no CuL^1 (green).

yielded comparable results, giving a slightly lower charge of 67.0 C, producing 3.5×10^{-4} moles of H_2 corresponding with a TON of 58.3.

The CPEs performed in 0.1 M Bu_4NPF_6 ACN passed similar charge, giving values of 60.4 and 84.7 C corresponding to TON values of 51.7 and 73.3 over shorter electrolysis times of 15 000 and 13 000 s, respectively (Figure 5). The current in ACN is significantly higher than that in DMF, resulting in a steeper slope in the charge-time plots, consistent with relative TOFs from CV studies. Electrolysis beyond 15 000 s in ACN is complicated by diffusion across the frit from the working to auxiliary compartment. This results in the appearance of a brown, cloudy mixture in the auxiliary compartment concurrent with the plateauing of charge. This phenomenon was consistently observed in ACN, but was absent in DMF.

Control Experiments. A series of control experiments was performed to confirm CuL^1 as the electrocatalyst. First, CVs were recorded on ACN and DMF solutions containing only

DOI: 10.1021/acs.inorgchem.7b01608
Inorg. Chem. 2017, 56, 11254−11265

acetic acid. Addition of 67.2 mM acetic acid to 0.1 M Bu_4NPF_6 ACN solutions resulted in an observable current of 300 μA (Figure 6A). However, after 2 CV cycles the current drops to a

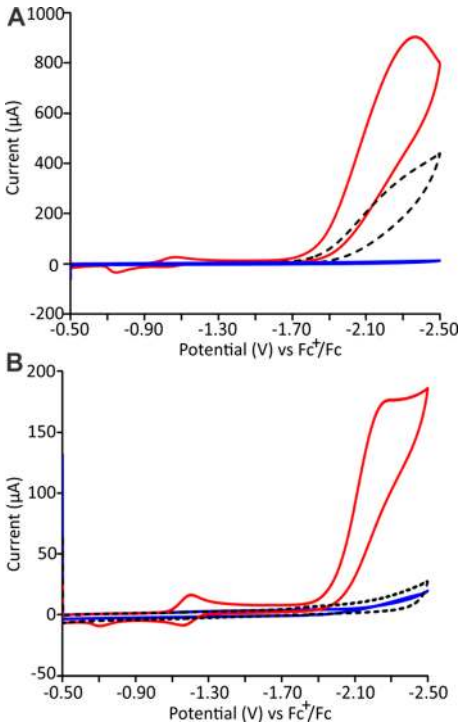

Figure 6. (A) CVs run in 0.1 M Bu_4NPF_6 ACN solutions, showing blank ACN (blue) with 0.0672 M acetic acid added (black dashed) and with 0.0672 M acetic acid and 0.6 mM CuL^1 (red). (B) CVs run in 0.1 M Bu_4NPF_6 DMF solutions, showing blank DMF (blue) with 0.0224 M acetic acid added (black dashed) and with 0.0224 M acetic acid and 0.6 mM CuL^1 (red).

stable value near 100 μA. Upon addition of 0.6 mM CuL^1, the current increases to 900 μA (Figure 6A). In DMF addition of 22.4 mM acetic acid results in a modest current increase of ~5 μA (Figure 6B). Addition of 0.6 mM CuL^1 to this solution resulted in an increase in current, giving a value of 200 μA (Figure 6B). This is in contrast to the report by Mauer et al. from 2002, where the authors state that in the presence of 0.0224 M acetic acid in DMF, CVs of CuL^1 show no observable change.[53] However, in the prior study, the scans were not extended beyond −1.0 V vs Ag wire (−1.60 V vs Fc^+/Fc). At more cathodic potentials, a substantial change in the CVs of CuL^1 with 22.4 mM acetic acid added is observed with an increase in current onset potentials near −1.7 V vs Fc^+/Fc (Figure 6B). These control experiments identify CuL^1 as the source of the catalytic activity but do not exclude the possibility that it may be the precursor to an adsorbed catalyst.[77−79]

To probe for adsorption of the CuL^1 on the electrode surface prior to catalysis, a soak test was performed using the methods of Dempsey and co-workers.[78] The working electrode was immersed overnight in a 0.1 M Bu_4NPF_6 ACN solution containing 0.6 mM CuL^1 and 0.292 M acetic acid. It was then removed, washed with DI water, and placed into a fresh solution of 0.1 M Bu_4NPF_6 ACN, with no added acid or catalyst. The resulting CV displayed no redox events, indicating no detectable adsorption of CuL^1 derived species under these conditions.

A second series of controls were performed to evaluate if a catalytically active adsorbed species forms during CV catalysis. These post-CV dip tests were conducted after 10 and 50 cycles. During the 50 cycles from −0.5 to −2.3 V vs Fc^+/Fc on 0.6 mM CuL^1 solutions under acid saturated conditions, the current reaches a maximum value of ~1.5 mA. The working electrode was removed, washed with DI water, and immersed into a fresh solution of 0.1 M Bu_4NPF_6 ACN or DMF. The resulting CVs showed no significant Faradaic current in the window from −0.5 to −2.3 V. Upon addition of 0.292 M acetic acid, a catalytic current of 1 mA was observed at −1. Notably, Holland et al.[54] previously reported a two electron stripping wave at 0.4 V vs SCE (−0.1 V vs Fc^+/Fc) following reduction of CuL^1 in the presence of HBF_4. The peak was assigned to oxidation of a surface adsorbed Cu(I) dimer, $[(CuL^1H_2)_2]^{2+}$. After we extended the scan window to include this event, the catalytic current at −1.7 V is absent. This confirms that at least some of the HER catalysis results from adsorbed CuL^1 species.

To probe if all the catalytic activity results from adsorbed catalysts, we repeated the post-CV dip test after 10 cycles from −0.5 to −2.5 V vs Fc^+/Fc on 0.6 mM CuL^1 solutions under acid saturated conditions, again reaching maximum current values of ~1.5 mA. The working electrode was removed, washed with DI water, and immersed into a fresh solution of 0.1 M Bu_4NPF_6 DMF. As before, the resulting CVs showed no observable Faradaic current in the window from −0.5 to −2.5 V. CVs following addition of 0.292 M acetic acid showed only 400 μA of current at −1.7 V. While these results indicate that surface adsorbed CuL^1 is responsible for some of the catalytic current after as few as 10 cycles, they clearly show that the majority of HER activity under homogeneous conditions is due to dissolved CuL^1 complex.

In addition, a postelectrolysis dip-test was performed following CPE studies of CuL^1 catalyzed HER. Under these conditions, a substantial amount of surface adsorbed CuL^1 derived complex is expected. After both CPEs in DMF and ACN, the working electrode was removed, washed with DI water, and immersed into a fresh 0.1 M Bu_4NPF_6 DMF/ACN solution. The CV was collected. In contrast to the post-CV dip tests, the electrode displays 3 reduction events at −0.9, −1.4, and −2.1 V vs Fc^+/Fc. The first two events are near the observed Cu(II/I) reduction potentials of $[CuL^1H]^+$ and CuL^1, respectively. The most cathodic event is near the reduction potential of H_2L^1.[28] Upon addition of 0.292 M acetic acid to the solution, current increases, and catalysis is observed (Figure 7).

Analysis of the films following electrolysis in DMF and ACN by X-ray photoelectron spectroscopy revealed atomic percentages consistent with CuL^1, Figure 8. While the data does not confirm intact CuL^1 in the film, it strongly suggests that the ligand and the metal are incorporated in the film in equal molar quantities. Further, high resolution XPS (see Supporting Information) confirms the presence of Cu ions in either the +1 or +2 charge state, which is inconsistent with the formation of metallic Cu nanoparticles. However, we cannot completely exclude the formation of oxidized copper nanoparticles such as Cu oxide infused with equimolar quantities of L^1 or some other organic component of similar elemental composition. The data from the two solvents are indistinguishable. On the basis of our electrochemical analysis and detailed control studies, it is evident that some of the observed catalysis is due to a homogeneous process, although we cannot estimate what amount is attributable to a heterogeneous process. Further

DOI: 10.1021/acs.inorgchem.7b01608
Inorg. Chem. 2017, 56, 11254−11265

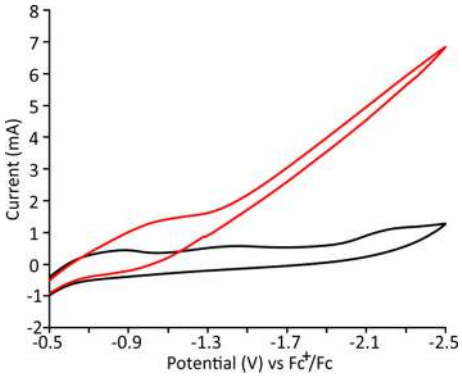

Figure 7. Postelectrolysis dip test performed on working electrode post CPE. The electrode was washed with DI water and immersed into a fresh solution of 0.1 M Bu_4NPF_6 ACN (black) upon addition of 0.292 M CH_3COOH (red).

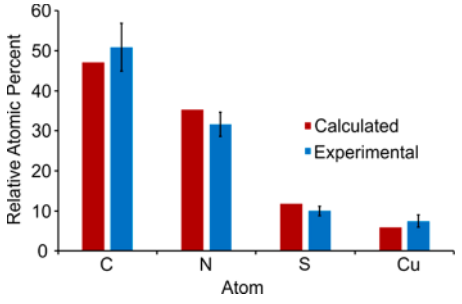

Figure 8. Calculated (red) and XPS experimental (blue) relative atomic mass percent for postelectrolysis CuL^1 derived films. Error bars show $\pm 3\sigma$ for 4 experimental measurements.

characterization and activity studies of CuL^1-based films are ongoing.

Protonated Derivatives of CuL^1. A series of protonated derivatives of CuL^1 was evaluated as potential catalytically relevant intermediates. These include the mono- and diprotonated Cu(II) complexes $[CuLH]^+$ and $[CuLH_2]^{2+}$ and the Cu(I) analogue CuLH. The Cu(II) complexes were previously observed spectroscopically and in electrochemical studies upon addition of HBF_4 to CuL^1.[54] The dinuclear Cu(I) complex $[(CuLH_2)_2]^{2+}$, which was previously characterized by single crystal X-ray diffraction,[80] was not considered as a catalytically relevant species under homogeneous conditions, as the reaction is first-order in CuL^1.

To confirm that protonation of the Cu(II) complex CuL^1 occurs under catalytic conditions prior to reduction, acid titrations were monitored by UV−visible spectroscopy. The spectrum of 0.6 mM CuL^1 in deoxygenated DMF shows absorbance bands at 310, 375, 475, and 520 nm. The solution was titrated with acetic acid, increasing in concentration from 0.022 to 0.382 M (Figure 9). The absorbance bands of CuL^1 decrease in intensity, concurrent with increases at 405 and 460 nm, consistent with the formation of $[CuL^1H]^+$.[54] The proposed protonation site is the hydrizino N, in line with previous reports and density functional theory computations (vide infra).

To characterize the reduced Cu(I) species, the Cu(II) complex CuL^1 was chemically reduced using cobaltocene and spectroscopically analyzed in the absence and presence of acid. The UV−visible spectrum (see Supporting Information) upon reduction in DMF is consistent with the formation of

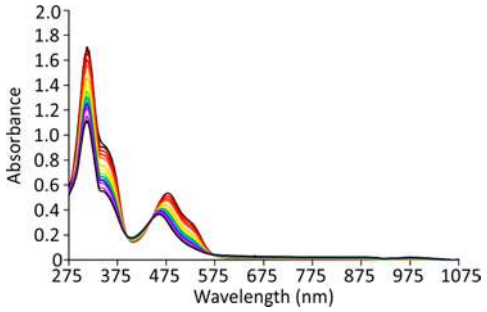

Figure 9. UV−visible spectra of CuL^1 titrated with CH_3COOH; 0.022 (dark red), 0.044 (red), 0.056 (light red), 0.067 (orange), 0.089 (light orange), 0.112 (yellow), 0.134 (light green), 0.157 (green), 0.202 (sky blue), 0.244 (blue), 0.269 (magenta), 0.292 (light blue), 0.337 (purple), and 0.382 (black) M.

$[CuL^1]^-$.[54] Addition of HPF_6 results in a decrease in band intensity at 360 and 505 nm. To further confirm the protonation of $[CuL^1]^-$, ^1H NMR spectra were collected in DMSO-d_6 (see Supporting Information). In the absence of acid, $[CuL^1]^-$ displays peaks at δ (ppm) = 1.99 (s, 6H) CCH_3, 2.66 (s, 6H) $NHCH_3$, and 5.72 (s, 2H) $NHCH_3$, which are similar to values reported for ZnL^1 in DMSO-d_6.[81] Addition of aqueous HPF_6 generates a spectrum consistent with the diprotonated Cu(I) complex $[CuL^1H_2]^+$. The ^1H NMR shows a new set of peaks at δ (ppm) = 2.07 (s, 6H) CCH_3, 3.03 (s, 6H) $NHCH_3$, 8.26 (s, 2H) $NHCH_3$, and 10.91 (s, 2H) NNH, which are similar to values for H_2L^1.[70]

The diprotonated Cu(II) complex $[CuL^1H_2]^{2+}$ was previously observed in CVs collected in the presence of HBF_4.[54] However, our CH_3COOH titration studies show no evidence of a second protonation event under catalytic conditions. Although $[CuL^1H_2]^{2+}$ is not catalytically relevant, X-ray quality crystals of $[CuL^1H_2]^{2+}$ were obtained from acetonitrile/methanol/perchloric acid solution. The ORTEP representation shows protonation of both hydrizino nitrogens, axial coordination of one perchlorate, and axial association of the second perchlorate, Figure 10. A complete description of the crystallographic details is provided in the Supporting Information.

Proposed Homogeneous HER Mechanism. A proposed CECE mechanism for homogeneous HER catalyzed by CuL^1 is shown in Scheme 3. Step 1 is an initial chemical (C) event involving protonation of the hydrazino nitrogen on CuL^1 to yield $[CuL^1H]^+$. This is followed by an electrochemical step (E) assigned as a metal-centered reduction giving the neutral Cu(I) species, CuL^1H. Step 3 is a chemical step involving protonation on the other hydrazino nitrogen, affording the Cu(I) cation, $[CuL^1H_2]^+$. Step 4 is the final electrochemical step, a proposed ligand-centered reduction to give the neutral species, CuL^1H_2. The CuL^1H_2 complex can be regarded as Cu(I) coordinated by a nitrogen-centered radical. Step 5 shows double bond rearrangement, resulting in an anionic coordinated nitrogen. This anionic nitrogen induces an internal proton transfer, a tautomerism that has been observed in many thiosemicarbazone complexes,[38,83−85] leading to formation of the H_2 evolving complex. Finally, in step 6, hydrogen is evolved through hydrogen atom or proton/hydride coupling at the adjacent N−H bonds.

The proposed mechanism is consistent with the experimentally determined rate law and the KIE proton inventory study. Both protons are added to a single CuL^1 complex prior

DOI: 10.1021/acs.inorgchem.7b01608
Inorg. Chem. 2017, 56, 11254−11265

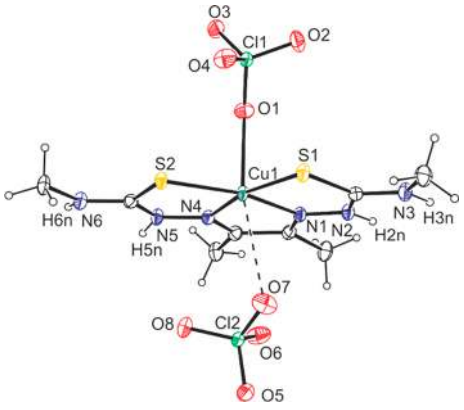

Figure 10. ORTEP[82] representation of $[Cu(L^1H_2)(ClO_4)]ClO_4$. Selected distances (Å): Cu1–N1 1.9579(18), Cu1–N4 1.9557(18), Cu1–S1 2.2462(6), Cu1–S2 2.2593(6), Cu1–O1 2.5166(16), Cu1···O7 2.9233(19), N2–H2n 0.78(3), N3–H3n 0.76(3), N4–N5 1.364(2), N5–H5n 0.78(2), N6–H6n 0.78(3). Selected angles (deg): N1–Cu1–N4 78.80(7), N1–Cu1–S1 86.88(6), N4–Cu1–S(2) 86.08(5), S1–Cu1–S2 108.02(2), N2–N1–Cu1 118.19(14), N1–N2–H2n 121(2), N5–N4–Cu1 119.13(14), N4–N5–H5n 119.9(19).

Scheme 3. Proposed Mechanism of Hydrogen Evolution by CuL^1

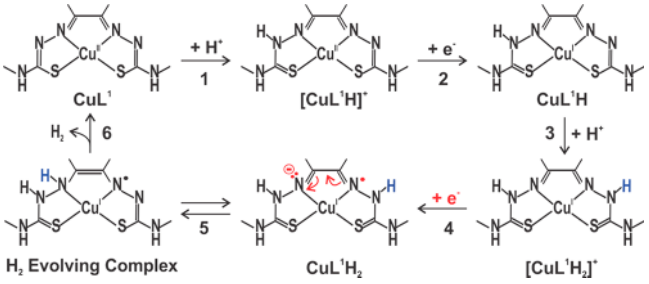

to the rate-determining step (rds), consistent with the first-order catalyst and second-order proton dependence on current. The proton inventory study suggests that a single proton is involved in the rds This is consistent with proton tautomerization, step 5, over hydrogen evolution, step 6, as the rate limiting event. The solvent dependency of the TOF further supports this interpretation. The TOF in DMF is approximately one-half that in ACN. This is attributed to H-bonding interactions between DMF and ligand N–H groups. These stabilizing interactions retard the rate limiting tautomerization step in DMF relative to ACN. To assess the viability of this mechanism, density functional theory computations on all proposed species were performed.

Density Functional Theory Investigations. All proposed complexes in Scheme 3 were assessed using DFT using the B3LYP functional[62] and the 6-311g(d,p) basis set. First, we evaluated the protonation event associated with step 1. Calculations on the singly protonated intermediate, $[CuL^1H]^+$, support our assignment of the hydrazino nitrogen as the site of protonation. For $[CuL^1H]^+$ (S = 1/2), the Cu, S, N3 (hydrazino), N4 (coordinated), and N6 (pendant amine) were evaluated as possible protonation sites. In each structure, the geometry and frequencies were optimized and the energies minimized. The hydrizino protonated geometry is energetically preferred, lying 10 kcal/mol lower than the metal-hydride (Figure 11A). Protonation at S is less favored by 12 kcal/mol

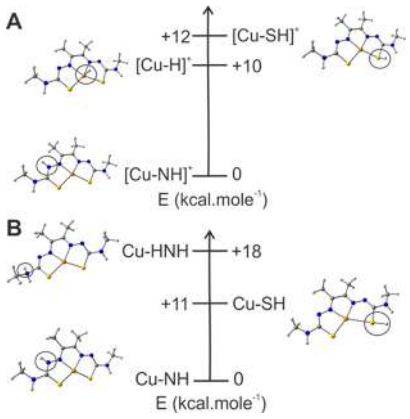

Figure 11. (A) Energetic stability of protonated species, $[CuL^1H]^+$ (S = 1/2). (B) Energetic stability of protonated/reduced species, CuL^1H (S = 0), B3LYP/6-311g(d,p).

and attempts to optimize structures with protonation on N4 and N6 resulted in migration of the hydrogen onto the hydrazino nitrogen.

Next, the one-electron reduced protonated species, CuL^1H (S = 0) (Figure 11B), was examined to determine if reduction, step 2, impacts the location of the proton. Computed free energies for structures with protonation at Cu, S, and each N, clearly indicate that protonation on the hydrazino N is still favored. Protonation at S is disfavored by 11 kcal/mol, while protonation at the pendant amine is less favored by 18 kcal/mol. Attempts to optimize CuL^1H with protonation at the coordinated nitrogen again resulted in migration of hydrogen onto the hydrazino nitrogen. We also considered CuL^1H with protonation on the hydrazino nitrogen in its triplet electronic configuration (S = 1). However, it is 5.77 kcal/mol higher in energy (Supporting Information), confirming the nature of the first reduction as metal-based.

Step 3 of the proposed mechanism involves addition of a second proton to CuL^1H. Energy minimizations of the doubly protonated, singly reduced intermediate, $[CuL^1H_2]^+$ in both the singlet (S = 0) and triplet (S = 1) electronic states were performed. For each spin state, the copper, the opposing hydrazino nitrogen (N1), sulfur (S2), the pendant amine (N6), and the coordinated nitrogen (N4) were all considered as the second protonation site. In both electronic states, protonation on the opposing hydrazino nitrogen (N1) is favored over all other protonation sites by at least 8 kcal/mol. Comparison of the singlet and triplet state the energies for protonation on N4 indicate the singlet is more stable by 6.09 kcal/mol (Figure 12).

The addition of the second electron, step 4, leads to formation of the hydrogen evolving complex CuL^1H_2 through proposed rearrangement, step 5. The geometry and frequencies of CuL^1H_2 were optimized with one proton located on N3 while considering multiple sites for the second proton,

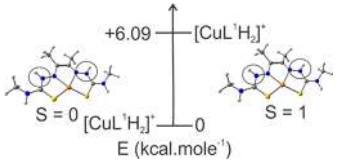

Figure 12. Energetic stability of the protonated/reduced/protonated species, $[CuL^1H_2]^+$, in the singlet (S = 0) and triplet (S = 1) electronic states, B3LYP/6-311g(d,p).

DOI: 10.1021/acs.inorgchem.7b01608
Inorg. Chem. 2017, 56, 11254–11265

including the copper, the opposing hydrazino nitrogen (N1), sulfur (S2), the pendant amine (N6), and the coordinated nitrogen (N4). Energy minimizations indicate that placement of the second proton on N1 or N4 nitrogen are most favored by at least 17 kcal/mol, compared to all other sites (Figure 13A). Notably, energies for protonation at N1 and N4 differ by

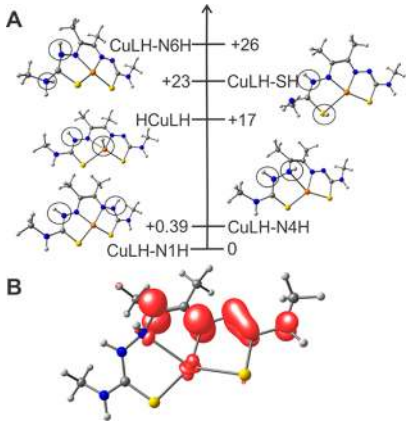

Figure 13. (A) Energetic stability of CuL^1H_2 (S = 1/2). (B) Spin-density map of CuL^1H_2 with second protonation on N4, B3LYP/6-311g(d,p).

only 0.39 kcal/mol, indicating that the tautomerization associated with step 5 in the proposed mechanism is viable. Further, examination of the spin-density (SD) shows that the second reduction is primarily ligand-based, with 34% on N2, 38% on C4, 14% on N1, 8% on N5, and only 3% on Cu (Figure 13B).

Discussion. Thiosemicarbazone ligands and their metal complexes are relatively new to the field of electrochemical proton reduction but are emerging as an important class of HER catalysts. The current work represents the fifth thiosemicarbazone motif to be reported as an active HER catalyst since the first report at the end of 2015.[28,52,86] These complexes present intriguing reactivity as the thiosemicarbazone ligand can participate in electron transfer events, either with or without a transition metal, rendering it noninnocent. Additionally, thiosemicarbazone ligands can be protonated generating various tautomeric forms, rendering it not only noninnocent, but also promiscuous. The combination of these two factors appears to be strongly dependent on the identity of the metal ion, resulting in the three distinct types of HER reactivity: (a) ligand-assisted metal reactivity with Ni, (b) ligand-centered reactivity with Zn, and (c) metal-assisted ligand reactivity with Cu.

The impact of the metal is manifested in the initial protonation and reduction sites. For both CuL^1 and ZnL^1, a hydrazino N is protonated prior to the initial reduction. For NiL^2, it is reported that ligand-centered reduction must precede protonation, which then occurs at a coordinated N.[52] The initial site of reduction can be rationalized based on the relative energies of the metal d-orbitals and an unoccupied ligand centered orbital, Scheme 4. The metal d-orbital energies decrease from Ni^{2+} to Cu^{2+} to Zn^{2+} with increasing effective nuclear charge. For Ni^{2+} there is a vacant ligand-centered orbital that lies below the vacant metal d_{z2} orbital, yielding a ligand-centered radical upon reduction. For Cu^{2+}, the stabilized d-orbital manifold falls below the ligand-centered orbital resulting in metal-centered reduction. For Zn^{2+}, the d-orbitals

Scheme 4. Qualitative Frontier Molecular Orbital Diagram Highlighting Site of Reduction

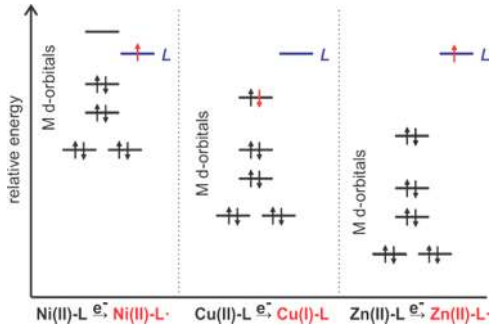

are filled requiring ligand-centered reduction. Additionally, the site of reduction and the localization of spin-density impact the site of protonation. For Cu, the proton remains on the hydrizino nitrogen after metal-centered reduction. In contrast, for Ni the ligand-centered reduction favors double bond rearrangement similar to step 5 in Scheme 3. As a result, the tautomers with protonation of the hydrizino N and anionic coordinated N have similar energies.[52] For Zn, the tautomer with the proton remaining on the hydrizino N remains favored after ligand-centered reduction.

The mechanism for H_2 evolution is a consequence of the initial protonation and reduction sites. For Ni, Straistari et al. posit that the second reduction is metal-based, generating a nucleophilic d^9 Ni(I) center. Further protonation is proposed to occur at the metal generating a Ni^{III}-hydride as the catalytically active species for H_2 evolution. In this context, NiL^2 demonstrates ligand-assisted metal reactivity, in which the ligand serves as an auxiliary redox site to facilitate two-electron chemistry at the metal. This is a common role for redox active ligands in transition-metal catalysis. In contrast, the HER chemistry of ZnL^1 is strictly ligand-centered. Its HER mechanism localizes all chemical and electrochemical steps on the ligand, with the metal providing structural support. As in the case of NiL^2, initial protonation and reduction is ligand-centered; however, the d^{10} Zn(II) is incapable of undergoing a second reduction, and HER proceeds via a bimolecular process.[28]

The HER chemistry of CuL^1 displays a less common type of mechanism with redox noninnocent ligands, which we defined as metal-assisted ligand-centered reactivity. The initial metal-centered reduction leads to a d^{10} Cu(I), which is isoelectronic with ZnL^1. As such, it can accommodate subsequent ligand-based protonation and reduction events with evolution of H_2 from the ligand-center. In this context, the metal serves as the auxiliary redox site, which facilitates two-electron chemistry at the ligand.

CONCLUSION

To the best of our knowledge, CuL^1 is the first HER electrocatalyst to demonstrate a metal-assisted ligand-centered mechanism. The redox noninnocence and protonation promiscuity of the thiosemicarbazone ligand framework provides for a variety of HER mechanisms that are dependent on the metal ion. The CuL^1 system exhibits the highest reported TOF of any ligand-centered homogeneous HER catalysts to date. However, its high activity requires large overpotential that limits its realistic application as a functional HER catalyst. Nonetheless, the metal-assisted ligand reactivity

DOI: 10.1021/acs.inorgchem.7b01608
Inorg. Chem. 2017, 56, 11254−11265

of CuL^1 provides a new template for future HER electrocatalysts that function without the participation of a metal-hydride. The current study demonstrates that noninnocent ligands can work in conjunction with a redox-active metal to promote ligand-centered reactivity. This represents a new approach to the development of electrocatalysts for HER and, possibly, the activation of other small molecules.

■ ASSOCIATED CONTENT

Supporting Information

The Supporting Information is available free of charge on the ACS Publications website at DOI: 10.1021/acs.inorgchem.7b01608.

Sample calculations, crystallographic details, NMR spectra, additional CV data, high resolution XPS spectra, computation input coordinates in PDF format, and crystallographic data (CCDC 1546071) (PDF)

Accession Codes

CCDC 1546071 contains the supplementary crystallographic data for this paper. These data can be obtained free of charge via www.ccdc.cam.ac.uk/data_request/cif, by emailing data_request@ccdc.cam.ac.uk, or by contacting The Cambridge Crystallographic Data Centre, 12 Union Road, Cambridge CB2 1EZ, UK; fax: +44 1223 336033.

■ AUTHOR INFORMATION

Corresponding Author

*E-mail craig.grapperhaus@louisville.edu.

ORCID

Andrew Z. Haddad: 0000-0002-9206-3505

Craig A. Grapperhaus: 0000-0003-4889-2645

Notes

The authors declare no competing financial interest.

■ ACKNOWLEDGMENTS

This research was supported in part by the National Science Foundation (Grant CHE-1361728) and a grant from the Kentucky Science and Engineering Foundation as Grant KSEF-148-502-15-350 with the Kentucky Science and Technology Corporation. The authors are thankful to Cardinal Research Cluster at the University of Louisville for providing the computational facilities. M.S.M. thanks the Department of Energy (Grant DE-FG02-08CH11538) and the Kentucky Research Challenge Trust Fund for the upgrade of our X-ray facilities. The authors are thankful to Yaroslav Losovyj at the Nanoscale Characterization Facility at the University of Indiana for collection of XPS data. Access to XPS at the Nanoscale Characterization Facility was provided by the NSF Award DMR MRI-1126394. The authors thank Wuyu Zhang for helpful discussions regarding XPS data interpretation. A.Z.H, R.M.B., and C.A.G. are inventors on a U.S. provisional patent application no. 62/348,420, filed by the University of Louisville Research Foundation, Inc., related to this work.

■ REFERENCES

(1) Cook, T. R.; Dogutan, D. K.; Reece, S. Y.; Surendranath, Y.; Teets, T. S.; Nocera, D. G. Solar Energy Supply and Storage for the Legacy and Nonlegacy Worlds. *Chem. Rev.* **2010**, *110*, 6474−6502.

(2) Lewis, N. S.; Nocera, D. G. Powering the Planet: Chemical Challenges in Solar Energy Utilization. *Proc. Natl. Acad. Sci. U. S. A.* **2006**, *103*, 15729−15735.

(3) Gray, H. B. Powering the Planet with Solar Fuel. *Nat. Chem.* **2009**, *1*, 7−7.

(4) Nocera, D. G. The Artificial Leaf. *Acc. Chem. Res.* **2012**, *45*, 767−776.

(5) Vesborg, P. C. K.; Seger, B.; Chorkendorff, I. Recent Development in Hydrogen Evolution Reaction Catalysts and Their Practical Implementation. *J. Phys. Chem. Lett.* **2015**, *6*, 951−957.

(6) Teets, T. S.; Nocera, D. G. Photocatalytic Hydrogen Production. *Chem. Commun.* **2011**, *47*, 9268−9274.

(7) Holton, O. T.; Stevenson, J. W. The Role of Platinum in Proton Exchange Membrane Fuel Cells. *Platinum Met. Rev.* **2013**, *57*, 259−271.

(8) McKone, J. R.; Marinescu, S. C.; Brunschwig, B. S.; Winkler, J. R.; Gray, H. B. Earth-Abundant Hydrogen Evolution Electrocatalysts. *Chem. Sci.* **2014**, *5*, 865−878.

(9) Simmons, T. R.; Berggren, G.; Bacchi, M.; Fontecave, M.; Artero, V. Mimicking Hydrogenases: From Biomimetics to Artificial Enzymes. *Coord. Chem. Rev.* **2014**, *270−271*, 127−150.

(10) Thoi, V. S.; Sun, Y.; Long, J. R.; Chang, C. J. Complexes of Earth-Abundant Metals For Catalytic Electrochemical Hydrogen Generation Under Aqueous Conditions. *Chem. Soc. Rev.* **2013**, *42*, 2388−2400.

(11) Coutard, N.; Kaeffer, N.; Artero, V. Molecular Engineered Nanomaterials for Catalytic Hydrogen Evolution and Oxidation. *Chem. Commun.* **2016**, *52*, 13728−13748.

(12) Brazzolotto, D.; Gennari, M.; Queyriaux, N.; Simmons, T. R.; Pécaut, J.; Demeshko, S.; Meyer, F.; Orio, M.; Artero, V.; Duboc, C. Nickel-Centred Proton Reduction Catalysis In A Model Of [NiFe] Hydrogenase. *Nat. Chem.* **2016**, *8*, 1054−1060.

(13) Kaeffer, N.; Chavarot-Kerlidou, M.; Artero, V. Hydrogen Evolution Catalyzed by Cobalt Diimine−Dioxime Complexes. *Acc. Chem. Res.* **2015**, *48*, 1286−1295.

(14) Tsay, C.; Yang, J. Y. Electrocatalytic Hydrogen Evolution under Acidic Aqueous Conditions and Mechanistic Studies of a Highly Stable Molecular Catalyst. *J. Am. Chem. Soc.* **2016**, *138*, 14174−14177.

(15) Zarkadoulas, A.; Field, M. J.; Papatriantafyllopoulou, C.; Fize, J.; Artero, V.; Mitsopoulou, C. A. Experimental and Theoretical Insight into Electrocatalytic Hydrogen Evolution with Nickel Bis-(aryldithiolene) Complexes as Catalysts. *Inorg. Chem.* **2016**, *55*, 432−444.

(16) Lei, H.; Fang, H.; Han, Y.; Lai, W.; Fu, X.; Cao, R. Reactivity and Mechanism Studies of Hydrogen Evolution Catalyzed by Copper Corroles. *ACS Catal.* **2015**, *5*, 5145−5153.

(17) Bacchi, M.; Veinberg, E.; Field, M. J.; Niklas, J.; Matsui, T.; Tiede, D. M.; Poluektov, O. G.; Ikeda-Saito, M.; Fontecave, M.; Artero, V. Artificial Hydrogenases Based on Cobaloximes and Heme Oxygenase. *ChemPlusChem* **2016**, *81*, 1083−1089.

(18) Armstrong, J. E.; Crossland, P. M.; Frank, M. A.; Van Dongen, M. J.; McNamara, W. R. Hydrogen Evolution Catalyzed By A Cobalt Complex Containing an Asymmetric Schiff-Base Ligand. *Dalton Trans.* **2016**, *45*, 5430−5433.

(19) DiRisio, R. J.; Armstrong, J. E.; Frank, M. A.; Lake, W. R.; McNamara, W. R. Cobalt Schiff-Base Complexes for Electrocatalytic Hydrogen Generation. *Dalton Trans.* **2017**, *46*, 10418−10425.

(20) McNamara, W. R.; Han, Z. J.; Alperin, P. J.; Brennessel, W. W.; Holland, P. L.; Eisenberg, R. A Cobalt-Dithiolene Complex for the Photocatalytic and Electrocatalytic Reduction of Protons. *J. Am. Chem. Soc.* **2011**, *133*, 15368−15371.

(21) McNamara, W. R.; Han, Z. J.; Yin, C. J.; Brennessel, W. W.; Holland, P. L.; Eisenberg, R. Cobalt-Dithiolene Complexes for the Photocatalytic and Electrocatalytic Reduction of Protons in Aqueous Solutions. *Proc. Natl. Acad. Sci. U. S. A.* **2012**, *109*, 15594−15599.

(22) Rakowski Dubois, M.; Dubois, D. L. Development of Molecular Electrocatalysts for CO_2 Reduction and H_2 Production/Oxidation. *Acc. Chem. Res.* **2009**, *42*, 1974−1982.

(23) Wiese, S.; Kilgore, U. J.; DuBois, D. L.; Bullock, R. M. $[Ni(PMe_2NPh_2)_2](BF_4)_2$ as an Electrocatalyst for H_2 Production. *ACS Catal.* **2012**, *2*, 720−727.

DOI: 10.1021/acs.inorgchem.7b01608
Inorg. Chem. 2017, 56, 11254−11265

(24) DuBois, D. L. Development of Molecular Electrocatalysts for Energy Storage. *Inorg. Chem.* **2014**, *53*, 3935−3960.
(25) Gan, L.; Groy, T. L.; Tarakeshwar, P.; Mazinani, S. K. S.; Shearer, J.; Mujica, V.; Jones, A. K. A Nickel Phosphine Complex as a Fast and Efficient Hydrogen Production Catalyst. *J. Am. Chem. Soc.* **2015**, *137*, 1109−1115.
(26) Rakowski DuBois, M.; DuBois, D. L. The Roles of The First And Second Coordination Spheres In The Design of Molecular Catalysts For H_2 Production and Oxidation. *Chem. Soc. Rev.* **2009**, *38*, 62−72.
(27) Jurss, J. W.; Khnayzer, R. S.; Panetier, J. A.; El Roz, K. A.; Nichols, E. M.; Head-Gordon, M.; Long, J. R.; Castellano, F. N.; Chang, C. J. Bioinspired Design of Redox-Active Ligands For Multielectron Catalysis: Effects Of Positioning Pyrazine Reservoirs on Cobalt For Electro- And Photocatalytic Generation of Hydrogen From Water. *Chem. Sci.* **2015**, *6*, 4954−4972.
(28) Haddad, A. Z.; Garabato, B. D.; Kozlowski, P. M.; Buchanan, R. M.; Grapperhaus, C. A. Beyond Metal-Hydrides: Non-Transition-Metal and Metal-Free Ligand-Centered Electrocatalytic Hydrogen Evolution and Hydrogen Oxidation. *J. Am. Chem. Soc.* **2016**, *138*, 7844−7847.
(29) Thompson, E. J.; Berben, L. A. Electrocatalytic Hydrogen Production By An Aluminum(III) Complex: Ligand-Based Proton And Electron Transfer. *Angew. Chem., Int. Ed.* **2015**, *54*, 11642−11646.
(30) Sherbow, T. J.; Fettinger, J. C.; Berben, L. A. Control of Ligand pKa Values Tunes the Electrocatalytic Dihydrogen Evolution Mechanism in a Redox-Active Aluminum(III) Complex. *Inorg. Chem.* **2017**, *56*, 8651−8660.
(31) Panetier, J. A.; Letko, C. S.; Tilley, T. D.; Head-Gordon, M. Computational Characterization of Redox Non-Innocence in Cobalt-Bis(Diaryldithiolene)-Catalyzed Proton Reduction. *J. Chem. Theory Comput.* **2016**, *12*, 223−230.
(32) Haddad, A. Z.; Kumar, D.; Ouch Sampson, K.; Matzner, A. M.; Mashuta, M. S.; Grapperhaus, C. A. Proposed Ligand-Centered Electrocatalytic Hydrogen Evolution and Hydrogen Oxidation at a Noninnocent Mononuclear Metal−Thiolate. *J. Am. Chem. Soc.* **2015**, *137*, 9238−9241.
(33) Lyaskovskyy, V.; de Bruin, B. Redox Non-Innocent Ligands: Versatile New Tools to Control Catalytic Reactions. *ACS Catal.* **2012**, *2*, 270−279.
(34) Chirik, P. J. Preface: Forum on Redox-Active Ligands. *Inorg. Chem.* **2011**, *50*, 9737−9740.
(35) Dzik, W. I.; van der Vlugt, J. I.; Reek, J. N. H.; de Bruin, B. Ligands that Store and Release Electrons during Catalysis. *Angew. Chem., Int. Ed.* **2011**, *50*, 3356−3358.
(36) Muckerman, J. T.; Polyansky, D. E.; Wada, T.; Tanaka, K.; Fujita, E. Water Oxidation by a Ruthenium Complex with Non-innocent Quinone Ligands: Possible Formation of an O−O Bond at a Low Oxidation State of the Metal. *Inorg. Chem.* **2008**, *47*, 1787−1802.
(37) Garrido-Barros, P.; Funes-Ardoiz, I.; Drouet, S.; Benet-Buchholz, J.; Maseras, F.; Llobet, A. Redox Non-innocent Ligand Controls Water Oxidation Overpotential in a New Family of Mononuclear Cu-Based Efficient Catalysts. *J. Am. Chem. Soc.* **2015**, *137*, 6758−6761.
(38) Kochem, A.; Gellon, G.; Jarjayes, O.; Philouze, C.; du Moulinet d'Hardemare, A.; van Gastel, M.; Thomas, F. Nickel(II) Radical Complexes of Thiosemicarbazone Ligands Appended by Salicylidene, Aminophenol and Aminothiophenol Moieties. *Dalton Trans.* **2015**, *44*, 12743−12756.
(39) Huff, C. A.; Kampf, J. W.; Sanford, M. S. Role of a Noninnocent Pincer Ligand in the Activation of CO2 at (PNN)Ru(H)(CO). *Organometallics* **2012**, *31*, 4643−4645.
(40) Nielsen, M.; Kammer, A.; Cozzula, D.; Junge, H.; Gladiali, S.; Beller, M. Efficient Hydrogen Production from Alcohols under Mild Reaction Conditions. *Angew. Chem., Int. Ed.* **2011**, *50*, 9593−9597.
(41) Ringenberg, M. R.; Kokatam, S. L.; Heiden, Z. M.; Rauchfuss, T. B. Redox-Switched Oxidation of Dihydrogen Using a Non-Innocent Ligand. *J. Am. Chem. Soc.* **2008**, *130*, 788−789.
(42) Jørgensen, C. K. Differences between the Four Halide Ligands, and Discussion Remarks on Trigonal-Bipyramidal Complexes, on Oxidation States, and on Diagonal Elements of One-Electron Energy. *Coord. Chem. Rev.* **1966**, *1*, 164−178.
(43) Borman, C. D.; Saysell, C. G.; Sokolowski, A.; Twitchett, M. B.; Wright, C.; Sykes, A. G. Reactivity of galactose oxidase. *Coord. Chem. Rev.* **1999**, *190*, 771−779.
(44) Volbeda, A.; Charon, M.-H.; Piras, C.; Hatchikian, E. C.; Frey, M.; Fontecilla-Camps, J. C. Crystal Structure of the Nickel-iron Hydrogenase from Desulfovibrio gigas. *Nature* **1995**, *373*, 580−587.
(45) Volbeda, A.; Garcin, E.; Piras, C.; de Lacey, A. L.; Fernandez, V. M.; Hatchikian, E. C.; Frey, M.; Fontecilla-Camps, J. C. Structure of the [NiFe] Hydrogenase Active Site: Evidence for Biologically Uncommon Fe Ligands. *J. Am. Chem. Soc.* **1996**, *118*, 12989−12996.
(46) Blanchard, S.; Neese, F.; Bothe, E.; Bill, E.; Weyhermüller, T.; Wieghardt, K. Square Planar vs Tetrahedral Coordination in Diamagnetic Complexes of Nickel(II) Containing Two Bidentate π-Radical Monoanions. *Inorg. Chem.* **2005**, *44*, 3636−3656.
(47) Blanchard, S.; Bill, E.; Weyhermüller, T.; Wieghardt, K. N,N-Coordinated π Radical Anions of S-Methyl-1-phenyl-isothiosemicarbazide in Two Five-Coordinate Ferric Complexes [FeIII(LMe•)2X] (X = CH3S-, Cl-). *Inorg. Chem.* **2004**, *43*, 2324−2329.
(48) Akbar Ali, M.; Bernhardt, P. V.; Brax, M. A. H.; England, J.; Farlow, A. J.; Hanson, G. R.; Yeng, L. L.; Mirza, A. H.; Wieghardt, K. The Trivalent Copper Complex of a Conjugated Bis-dithiocarbazate Schiff Base: Stabilization of Cu in Three Different Oxidation States. *Inorg. Chem.* **2013**, *52*, 1650−1657.
(49) Kowol, C. R.; Reisner, E.; Chiorescu, I.; Arion, V. B.; Galanski, M.; Deubel, D. V.; Keppler, B. K. An Electrochemical Study of Antineoplastic Gallium, Iron and Ruthenium Complexes with Redox Noninnocent α-N-Heterocyclic Chalcogensemicarbazones. *Inorg. Chem.* **2008**, *47*, 11032−11047.
(50) Zhang, W.; Haddad, A. Z.; Garabato, B. D.; Kozlowski, P. M.; Buchanan, R. M.; Grapperhaus, C. A. Translation of Ligand-Centered Hydrogen Evolution Reaction Activity and Mechanism of a Rhenium-Thiolate from Solution to Modified Electrodes: A Combined Experimental and Density Functional Theory Study. *Inorg. Chem.* **2017**, *56*, 2177−2187.
(51) Solis, B. H.; Maher, A. G.; Dogutan, D. K.; Nocera, D. G.; Hammes-Schiffer, S. Nickel Phlorin Intermediate Formed by Proton-Coupled Electron Transfer in Hydrogen Evolution Mechanism. *Proc. Natl. Acad. Sci. U. S. A.* **2016**, *113*, 485−492.
(52) Straistari, T.; Fize, J.; Shova, S.; Réglier, M.; Artero, V.; Orio, M. A Thiosemicarbazone−Nickel(II) Complex as Efficient Electrocatalyst for Hydrogen Evolution. *ChemCatChem* **2017**, *9*, 2262−2268.
(53) Maurer, R. I.; Blower, P. J.; Dilworth, J. R.; Reynolds, C. A.; Zheng, Y.; Mullen, G. E. D. Studies on the Mechanism of Hypoxic Selectivity in Copper Bis(Thiosemicarbazone) Radiopharmaceuticals. *J. Med. Chem.* **2002**, *45*, 1420−1431.
(54) Holland, J. P.; Barnard, P. J.; Collison, D.; Dilworth, J. R.; Edge, R.; Green, J. C.; McInnes, E. J. L. Spectroelectrochemical and Computational Studies on the Mechanism of Hypoxia Selectivity of Copper Radiopharmaceuticals. *Chem. - Eur. J.* **2008**, *14*, 5890−5907.
(55) Fourmond, V.; Jacques, P. A.; Fontecave, M.; Artero, V. H_2 Evolution and Molecular Electrocatalysts: Determination of Overpotentials and Effect of Homoconjugation. *Inorg. Chem.* **2010**, *49*, 10338−10347.
(56) Wilson, A. D.; Newell, R. H.; McNevin, M. J.; Muckerman, J. T.; DuBois, M. R.; DuBois, D. L. Hydrogen Oxidation and Production Using Nickel-Based Molecular Catalysts with Positioned Proton Relays. *J. Am. Chem. Soc.* **2006**, *128*, 358−366.
(57) Bard, J. A.; Faulkner, R. L. *Electrochemical Methods: Fundamentals and Applications*, 2nd ed.; Wiley: Somerset, NJ, 2001.
(58) Appel, A. M.; DuBois, D. L.; DuBois, M. R. Molybdenum-Sulfur Dimers as Electrocatalysts for The Production Of Hydrogen At Low Overpotentials. *J. Am. Chem. Soc.* **2005**, *127*, 12717−12726.
(59) Lee, K. J.; Elgrishi, N.; Kandemir, B.; Dempsey, J. L. Electrochemical and spectroscopic methods for evaluating molecular electrocatalysts. *Nat. Rev. Chem.* **2017**, *1*, 0039.

DOI: 10.1021/acs.inorgchem.7b01608
Inorg. Chem. 2017, 56, 11254−11265

(60) Costentin, C.; Passard, G.; Savéant, J.-M. Benchmarking of Homogeneous Electrocatalysts: Overpotential, Turnover Frequency, Limiting Turnover Number. *J. Am. Chem. Soc.* **2015**, *137*, 5461−5467.
(61) Artero, V.; Savéant, J.-M. Toward The Rational Benchmarking of Homogeneous H_2-Evolving Catalysts. *Energy Environ. Sci.* **2014**, *7*, 3808−3814.
(62) Grimme, S. Semiempirical Gga-Type Density Functional Constructed With A Long-Range Dispersion Correction. *J. Comput. Chem.* **2006**, *27*, 1787−1799.
(63) Zhao, Y.; Truhlar, D. G. The M06 Suite of Density Functionals for Main Group Thermochemistry, Thermochemical Kinetics, Noncovalent Interactions, Excited States, and Transition Elements: Two New Functionals and Systematic Testing of Four M06-Class Functionals and 12 Other Functionals. *Theor. Chem. Acc.* **2008**, *120*, 215−241.
(64) Becke, A. D. Density-Functional Thermochemistry. III. The Role of Exact Exchange. *J. Chem. Phys.* **1993**, *98*, 5648−5652.
(65) Lee, C.; Yang, W.; Parr, R. G. Development of The Colle-Salvetti Correlation-Energy Formula Into A Functional of The Electron Density. *Phys. Rev. B: Condens. Matter Mater. Phys.* **1988**, *37*, 785−789.
(66) Vosko, S. H.; Wilk, L.; Nusair, M. Accurate Spin-Dependent Electron Liquid Correlation Energies for Local Spin Density Calculations: A Critical Analysis. *Can. J. Phys.* **1980**, *58*, 1200−1211.
(67) Stephens, P. J.; Devlin, F. J.; Chabalowski, C. F.; Frisch, M. J. Ab Initio Calculation of Vibrational Absorption and Circular Dichroism Spectra Using Density Functional Force Fields. *J. Phys. Chem.* **1994**, *98*, 11623−11627.
(68) Frisch, M. J.; Trucks, G. W.; Schlegel, H. B.; Scuseria, G. E.; Robb, M. A.; Cheeseman, J. R.; Scalmani, G.; Barone, V.; Mennucci, B.; Petersson, G. A.; Nakatsuji, H.; Caricato, M.; Li, X.; Hratchian, H. P.; Izmaylov, A. F.; Bloino, J.; Zheng, G.; Sonnenberg, J. L.; Hada, M.; Ehara, M.; Toyota, K.; Fukuda, R.; Hasegawa, J.; Ishida, M.; Nakajima, T.; Honda, Y.; Kitao, O.; Nakai, H.; Vreven, T.; Montgomery, Jr., J. A.; Peralta, J. E.; Ogliaro, F.; Bearpark, M. J.; Heyd, J.; Brothers, E. N.; Kudin, K. N.; Staroverov, V. N.; Kobayashi, R.; Normand, J.; Raghavachari, K.; Rendell, A. P.; Burant, J. C.; Iyengar, S. S.; Tomasi, J.; Cossi, M.; Rega, N.; Millam, N. J.; Klene, M.; Knox, J. E.; Cross, J. B.; Bakken, V.; Adamo, C.; Jaramillo, J.; Gomperts, R.; Stratmann, R. E.; Yazyev, O.; Austin, A. J.; Cammi, R.; Pomelli, C.; Ochterski, J. W.; Martin, R. L.; Morokuma, K.; Zakrzewski, V. G.; Voth, G. A.; Salvador, P.; Dannenberg, J. J.; Dapprich, S.; Daniels, A. D.; Farkas, Ö.; Foresman, J. B.; Ortiz, J. V.; Cioslowski, J.; Fox, D. J. *Gaussian 09*; Gaussian, Inc.: Wallingford, CT, 2009.
(69) Andrienko, G. ChemCraft Graphics Visualization Software. http://www.chemcraftprog.com (accessed November 2015).
(70) Christlieb, M.; Struthers, H. S. R.; Bonnitcha, P. D.; Cowley, A. R.; Dilworth, J. R. The Exocyclic Functionalisation of Bis-(Thiosemicarbazonate) Complexes Of Zinc And Copper: The Synthesis of Monomeric and Dimeric Species. *Dalton Trans.* **2007**, 5043−5054.
(71) Betts, H. M.; Barnard, P. J.; Bayly, S. R.; Dilworth, J. R.; Gee, A. D.; Holland, J. P. Controlled Axial Coordination: Solid-Phase Synthesis and Purification of Metallo-Radiopharmaceuticals. *Angew. Chem., Int. Ed.* **2008**, *47*, 8416−8419.
(72) Hu, X. L.; Brunschwig, B. S.; Peters, J. C. Electrocatalytic Hydrogen Evolution at Low Overpotentials by Cobalt Macrocyclic Glyoxime and Tetraimine Complexes. *J. Am. Chem. Soc.* **2007**, *129*, 8988−8998.
(73) Andrieux, C. P.; Blocman, C.; Dumasbouchiat, J. M.; M'Halla, F.; Savéant, J. M. Homogeneous Redox Catalysis of Electrochemical Reactions 0.5. Cyclic Voltammetry. *J. Electroanal. Chem. Interfacial Electrochem.* **1980**, *113*, 19−40.
(74) Savéant, J. M.; Su, K. B. Homogeneous Redox Catalysis of Electrochemical Reaction 6. Zone Diagram Representation Of The Kinetic Regimes. *J. Electroanal. Chem. Interfacial Electrochem.* **1984**, *171*, 341−349.
(75) Marinescu, S. C.; Winkler, J. R.; Gray, H. B. Molecular Mechanisms of Cobalt-Catalyzed Hydrogen Evolution. *Proc. Natl. Acad. Sci. U. S. A.* **2012**, *109*, 15127−15131.
(76) Venkatasubban, K. S.; Schowen, R. L. The proton inventory technique. *Crit. Rev. Biochem.* **1984**, *17*, 1−44.
(77) Kaeffer, N.; Morozan, A.; Fize, J.; Martinez, E.; Guetaz, L.; Artero, V. The Dark Side of Molecular Catalysis: Diimine−Dioxime Cobalt Complexes Are Not the Actual Hydrogen Evolution Electrocatalyst in Acidic Aqueous Solutions. *ACS Catal.* **2016**, *6*, 3727−3737.
(78) Lee, K. J.; McCarthy, B. D.; Rountree, E. S.; Dempsey, J. L. Identification of an Electrode-Adsorbed Intermediate in the Catalytic Hydrogen Evolution Mechanism of a Cobalt Dithiolene Complex. *Inorg. Chem.* **2017**, *56*, 1988−1998.
(79) McCarthy, B. D.; Donley, C. L.; Dempsey, J. L. Electrode initiated proton-coupled electron transfer to promote degradation of a nickel(ii) coordination complex. *Chem. Sci.* **2015**, *6*, 2827−2834.
(80) Cowley, A. R.; Dilworth, J. R.; Donnelly, P. S.; Labisbal, E.; Sousa, A. An Unusual Dimeric Structure of a Cu(I) Bis-(thiosemicarbazone) Complex: Implications for the Mechanism of Hypoxic Selectivity of the Cu(II) Derivatives. *J. Am. Chem. Soc.* **2002**, *124*, 5270−5271.
(81) Acta Crystallographica Section C Betts, H. M.; Barnard, P. J.; Bayly, S. R.; Dilworth, J. R.; Gee, A. D.; Holland, J. P. Controlled Axial Coordination: Solid-Phase Synthesis and Purification of Metallo-Radiopharmaceuticals. *Angew. Chem., Int. Ed.* **2008**, *47*, 8416−8419.
(82) Farrugia, L. ORTEP-3 for Windows - a version of ORTEP-III with a Graphical User Interface (GUI). *J. Appl. Crystallogr.* **1997**, *30*, 565.
(83) Donnelly, P. S.; Paterson, B. M. Process for the preparation of asymmetrical bis(thiosemicarbazones). Google Patents US20110305632A1, 2015.
(84) Gingras, B. A.; Suprunchuk, T.; Bayley, C. H. The preparation of some thiosemicarbazones and their copper complexes: Part iii. *Can. J. Chem.* **1962**, *40*, 1053−1059.
(85) Fusetto, R.; White, J. M.; Hutton, C. A.; O'Hair, R. A. J. Structure of olefin-imidacloprid and gas-phase fragmentation chemistry of its protonated form. *Org. Biomol. Chem.* **2016**, *14*, 1715−1726.
(86) Jing, X.; Wu, P.; Liu, X.; Yang, L.; He, C.; Duan, C. Light-Driven Hydrogen Evolution With A Nickel Thiosemicarbazone Redox Catalyst Featuring Ni···H Interactions Under Basic Conditions. *New J. Chem.* **2015**, *39*, 1051−1059.

DOI: 10.1021/acs.inorgchem.7b01608
Inorg. Chem. 2017, 56, 11254−11265